Long-term simulation of the boundary layer flow over the double-ridge site during the Perdigão 2017 field campaign

Johannes Wagner[1]**, Thomas Gerz**[1]**, Norman Wildmann**[1]**, and Kira Gramitzky**[1]

[1]Deutsches Zentrum für Luft- und Raumfahrt, Institut für Physik der Atmosphäre, 82234 Oberpfaffenhofen, Germany

5 *Correspondence to:* Johannes Wagner (johannes.wagner@dlr.de)

Abstract. The Perdigão campaign 2017 was an international field campaign to measure the flow and its diurnal variation in the atmospheric boundary layer over complex terrain. A huge dataset of meteorological observations was collected over the double-hill site by means of state-of-the-art meteorological measurement techniques. A focus of the campaign was the interaction of the boundary layer flow with a single wind turbine, which was located on the south-western (SW) ridge top.

10 In this study a long-term nested large-eddy-simulation (LES) of 49 days duration with a maximum horizontal resolution of 200 m is used to describe both the general meteorological situation over Spain and Portugal and the local small-scale flow structures over the double-hill during the intensive observation period (IOP). The simulations show that frequently observed nocturnal low-level jets (LLJ) from NE have their origin over the slopes of the elevated plateau between the Portuguese Serra da Estrela and the Spanish Sierra de Gata mountain ranges N and NE of Perdigão and that the diurnal clockwise turning of the

15 wind direction over the double-ridge is induced by slope- and valley-winds under weak synoptic conditions. It is found that in spite of the long simulation time, modelled and observed wind structures on the ridge tops agree well, while along-valley flow within the valley is underestimated by the model.

2

1   Introduction

The generation of electrical power from wind turbines (WT) is a worldwide fast growing industry and a key technique to extend

renewable energies (Emeis, 2013). Most of the areas that are available for onshore wind parks in flat terrain have already been

exploited on the European continent and further wind farms need to be installed in topographically complex terrain (Schulz

et al., 2014). The precondition to operate wind farms economically under these conditions is the ability to understand and

simulate the planetary boundary layer (PBL) flow in complex terrain and its interaction with WTs (Tian et al., 2013). A large

number of flow phenomena, such as thermally driven flows, gravity wave induced downslope wind storms and rotors are

common over complex terrain and difficult to simulate with numerical models. Of special interest for wind park operators is

the improved forecast of low-level jets (LLJs) (Storm et al., 2009). These are a worldwide phenomenon occuring where a local

wind maximum is observed close to the ground and they can develop both over large areas (e.g., the Great Plains in the US,

Rife et al., 2010) and very localized over complex terrain regions (e.g., within small valleys and basins, Banta et al., 2004).

LLJs are important for the formation of heavy precipitation events and for the transport of dust and aerosols over large distances

(Monaghan et al., 2010). Moreover, they are a significant source for wind power generation due to increasing WT hub heights.

Due to the shallow structure of the mostly nocturnal jets, the correct simulation of LLJs with operational weather models is

a challenge. It requires a sufficiently high horizontal and vertical grid resolution and a realistic representation of geographic

features, such as topography, landuse and surface roughness in the models.

In order to provide a new data set of PBL-flow over complex terrain including the interaction with a single WT, the interna-

tional field campaign Perdigão 2017 was organized in the context of the project "New European Wind Atlas" (NEWA, Mann

et al., 2017) to measure the flow over a nearly parallel double-hill topography in the Portuguese back country (Fernando et al.,

2018). The double-ridge site was chosen as it allows a smooth transition from idealized to complex terrain. This simplifies

the application of both idealized and realistic numerical modelling. In addition, the region around Perdigão is known for its

frequent occurence of diurnally changing NE and SW flow, which might be induced by thermally driven LLJs. The massive

instrumentation during the intensive observation period (IOP) of the field campaign with i.a. up to 49 meteorological towers,

28 Doppler wind lidars and 6-hourly radiosonde launches, provided a huge data set of meteorological observations, which can

be used to test and verify numerical simulations. In this study a long-term lare-eddy-simulation (LES) is used to characterize

the meteorological conditions and to identify dominant flow patterns during the IOP with a focus on LLJ-events. Observational

data are used to verify simulation results and to reveal potential for model improvement.

Atmospheric
Chemistry
and Physics
Discussions

Open Access
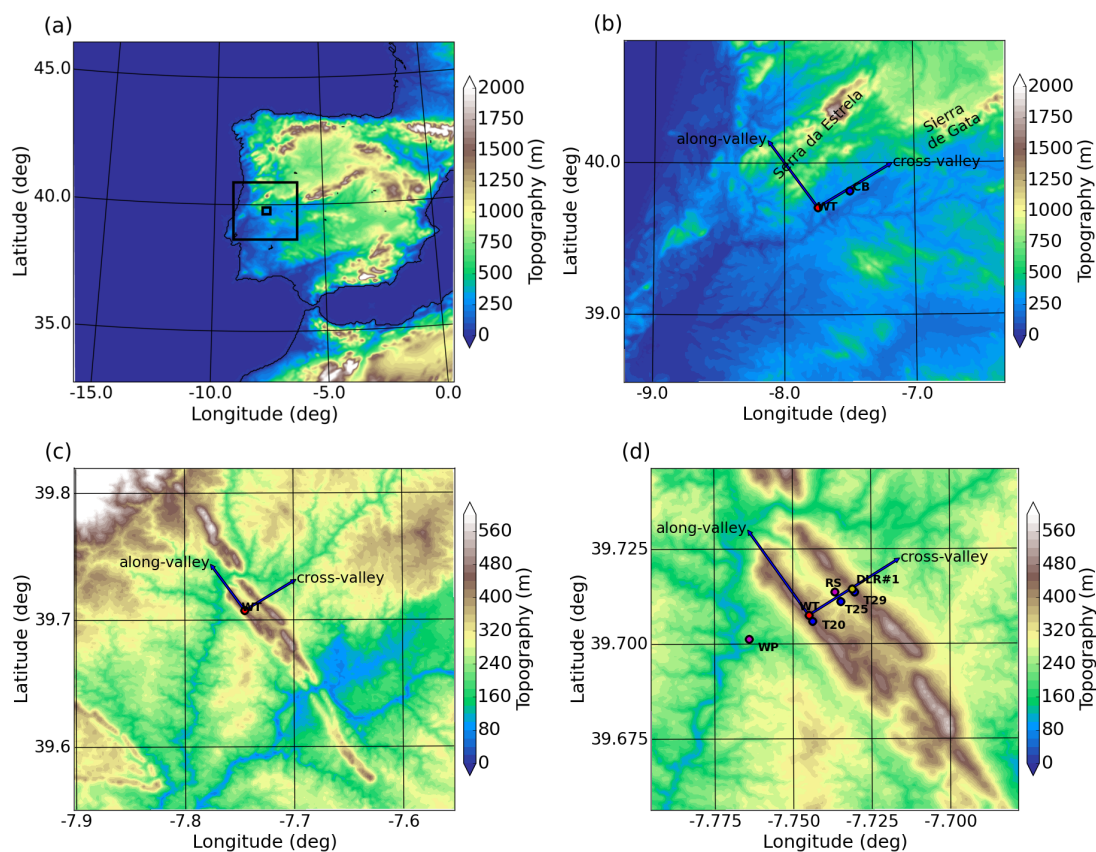
Figure 1. Topographic map of Spain and Portugal and operational area of the Perdigão field campaign. The shown areas in (a) mark the modelling domains D1 to D3. In (b) and (c) the topography of domain D2 and D3 is shown. The red dot marks the position of the wind turbine (WT) on the SW ridge and the town Castelo Branco (CB) is marked with a blue dot in (b). In (d) the double-ridge of domain D3 is enlarged to indicate the location of the WT, the three 100 m towers T20 (tower 20/tse04), T25 (tower 25/tse09) and T29 (tower 29/tse13), the Doppler wind lidar DLR#1, the wind profiler (WP) and the launch site of the radiosondes (RS). The blue perpendicular arrows in (b) to (d) mark cross- and along-valley wind directions. Cross-valley winds are defined by the location of the WT and the wind lidar DLR#1.

The paper is organized as follows: in section 2 the set-up of the numerical model is described. Dominating meteorological flow patterns during the field campaign are presented in section 3 and simulation results are compared to observations in section 4. A conclusion is given in section 5.

Atmospheric
Chemistry
and Physics
Discussions

4
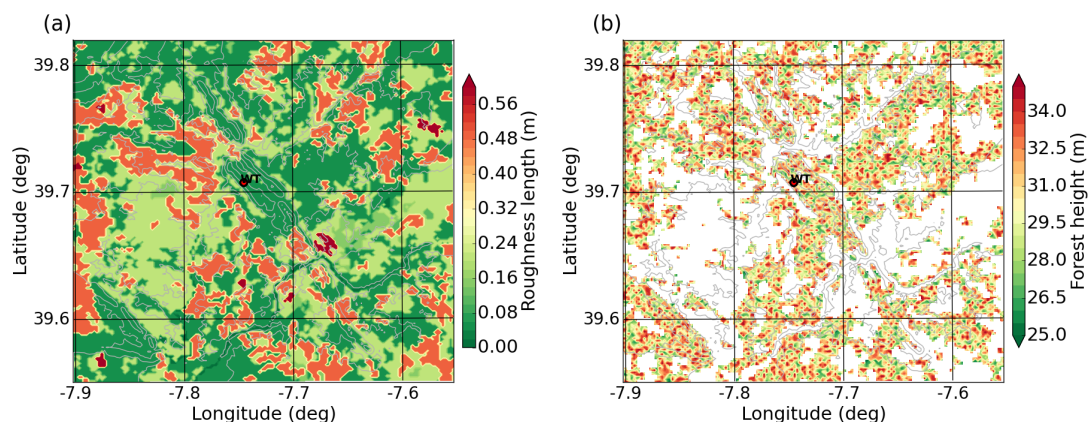
Figure 2. Surface roughness length of (a) the CORINE data set and (b) tree heights of the additionally implemented forest friction term applied to domain D3. White areas are not covered by forest. The location of the WT is marked with the red dot and the topography is indicated with grey contour lines.

2   Set-up of the numerical model

In this study, a long-term simulation is performed with the Weather Research and Forecasting (WRF) model version 3.8 (Skamarock et al., 2008). Three nested domains (D1, D2, and D3) with horizontal resolutions of 5 km, 1 km and 200 m are used (see Fig. 1). Domain D1 and D2 are run in RANS (Reynolds Averaged Navier Stokes) mode, while domain D3 is run in LES mode (see below for details on differences between these two modes). Vertical nesting is applied to define individual levels in the vertical for each model domain. This helps to avoid large grid aspect ratios near the surface and to save computational resources (Daniels et al., 2016). For domain D1 to D3 36, 57 and 70 vertically stretched levels are used and the respective lowest model levels are set to 80 m, 50 m and 15 m above ground level (AGL). The model top is defined at 200 hPa (about 12 km height) to include radiation and cloud effects at the tropopause. At the model top a 3 km thick Rayleigh damping layer (Klemp et al., 2008) is applied to prevent wave reflection. Physical parameterizations contain the Rapid Radiative Transfer Model longwave scheme (Mlawer et al., 1997), the Dudhia shortwave scheme (Dudhia, 1989), the Yonsei University (YSU) boundary layer scheme (Hong et al., 2006), the Noah land surface model (Chen and Dudhia, 2001), the WRF single-moment 5-class microphysics scheme (WSM5, Hong et al., 2004; Hong and Lim, 2006) and the Kain-Fritsch cumulus parameterization scheme (Kain and Fritsch, 1990). In domain D3 the boundary layer and cumulus schemes are switched off (LES mode) and subgrid-scale turbulence is parameterized by a three-dimensional 1.5 order turbulent kinetic energy (TKE) closure (Deardorff,

Atmospheric
Chemistry
and Physics
Discussions

Table 1. Overview of the WRF model set-up. Variables indicate the horizontal resolution (Δx) and the minimum distance of levels in the vertical near the surface (Δz_{min}). The number of grid points in x, y, and z direction is marked with nx, ny and nz, respectively.

Domain	Δx	Δz_{min}	nx×ny×nz	PBL scheme	Topography	Landuse	Forest param.	Forest height
D1	5 km	80 m	300×300×36	YSU	GTOPO30	USGS	no	-
D2	1 km	50 m	251×251×57	YSU	GTOPO30	USGS	no	-
D3	200 m	15 m	151×151×70	-	ASTER	CORINE	yes	30 m±5 m

1980). The simulation is initialized once at 00 UTC 30 April 2017 and run for 49 days and 18 hours until 18 UTC 18 June 2017. The initial and boundary conditions are supplied by ECMWF operational analyses on 137 model levels with a horizontal resolution of 8 km and a temporal resolution of 6 hours. The WRF output interval was set to 10 minutes to allow a better comparison with tower measurements.

For domain D1 and D2, the Global 30 Arc-Second Elevation (GTOPO30) digital elevation model and the U.S. Geological Survey (USGS) landuse data set are used. These are provided by the WRF preprocessing system (WPS). For domain D3, the Advanced Spaceborne Thermal Emission and Reflection Radiometer (ASTER) topography data set (Schmugge et al., 2003) with a horizontal resolution of 30 m and the Coordination of Information on the Environment (CORINE) land cover data with a horizontal resolution of 100 m is used to better resolve the double-ridge topography and landcover of the Perdigão region. The CORINE landuse categories were transformed into the 24 USGS WRF landuse types according to Pineda et al. (2004). The inspection of surface roughness lengths from CORINE landuse data indicates that roughness lengths are considerably too small. For example, Fig. 2(a) shows that CORINE roughness lengths are in the order of 0.1 m over the double-ridge. In reality the hills were partially covered by eucalyptus trees with heights of about 20 m to 25 m, which should be represented by roughness lengths in the order of 1 to 2 m. Short-term standard WRF simulations of LLJ-cases over Perdigão were run for 12 hours and showed that surface winds were clearly too high over the double-ridge region compared to lidar measurements (results will be shown in a successive paper). This was improved by the implementation of an additional friction term in the LES domain D3 in form of the forest parameterization described by Shaw and Schumann (1992), which acts on the lowermost model levels. The friction term was activated on grid points, which were classified as forest in the CORINE landuse data set (see Fig.2(b)). Tree heights in these forest areas were randomly distributed by 30 m ± 5 m and were defined somewhat higher

Atmospheric
Chemistry
and Physics
Discussions

6

in the model compared to real tree heights (about 25 m) to ensure that at least the lowermost 2 to 3 model levels are located

within the canopy layer. An overview of the described model set-up is shown in Table 1.

3   Meteorological flow patterns during the field campaign

The IOP of the Perdigão field campaign took place from 1 May to 15 June 2017 (Fernando et al., 2018). The instrumentation

was based on 49 meteorological towers (UCAR/NCAR - Earth Observing Laboratory, 2017a) with heights between 10 m to

100 m, more than 180 sonic anemometers, 21 scanning and 7 profiling wind lidars (e.g., Wildmann et al., 2018b), 3 microwave

radiometers (MWR), a radio acoustic sounding system (RASS) wind profiler (WP, UCAR/NCAR - Earth Observing Labora-

tory, 2017b) and 6-hourly radiosonde (RS, UCAR/NCAR - Earth Observing Laboratory, 2018) launches. On the southwestern

(SW) ridge, an Enercon E-82 2 MW WT with a hub-height of 78 m and a rotor diameter of 82 m is located (see Fig. 1).

Sound propagation and immission was measured by 9 microphones on the up- and downstream side of the SW ridge. In this

study, data of the wind profiler (WP), radiosonde (RS) observations and tower measurements of tower T20 (tower 20/tse04),

T25 (tower 25/tse09) and T29 (tower 29/tse13) were used (see Fig. 1). As the main wind directions at Perdigão are NE and

SW-flow, the focus in this study is on flow perpendicular (cross-valley) and parallel (along-valley) to the double-ridge. The

direction of cross- and along-valley winds is marked with the blue arrows in Fig. 1(b) to (d). Cross-valley winds were defined

along the cross-section of the DLR#1 wind lidar and is therefore not perfectly perpendicular to the double-ridge. Along-valley

winds are defined to be perpendicular to cross-valley winds. Negative cross- and along-valley winds mean winds from NE and

NW directions, respectively.

To give an overview of the meteorological conditions during the campaign, a WRF meteogram of domain D3 for the location

of the WT is shown in Fig. 3. Based on the synoptic conditions, the campaign can be divided into two phases. During the first

phase from 1 May to about 23 May the Perdigão region was influenced by periodic passages of low and high pressure systems,

as is visible from the surface pressure time series. Low pressure systems were accompanied by precipitation events, increased

cloudiness, reduced diurnal surface temperature variation and cross-valley winds at 10 m AGL from SW (wind direction sector

marked with red shading in Fig. 3). During high pressure events, surface winds were decoupled from the free atmosphere

during the night and thermally driven LLJs from NE developed (wind direction sector marked with blue shading in Fig. 3),

e.g., in the period from 2 to 3 May, 7 to 8 May or 16 to 17 May. Wind speed and wind direction at 500 hPa represent the
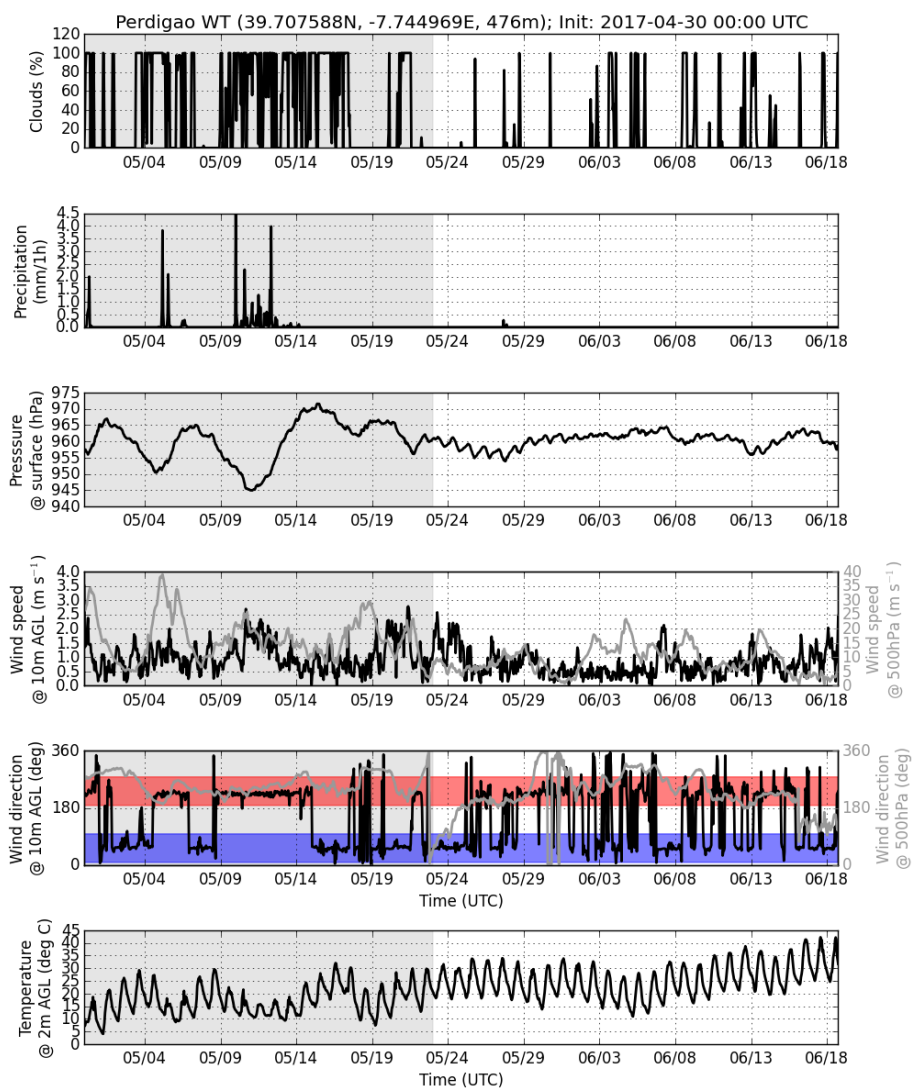
Figure 3. WRF D3 meteogram for 30 April to 18 June 2017 at the location of the WT on the SW ridge. The red and blue shaded areas in the wind direction plot mark cross-valley surface winds from SW and NE directions, respectively. The grey shading separates the campaign synoptically into phase I and phase II.

conditions in the free atmosphere and show that winds were blowing from western directions throughout the first phase of the campaign.
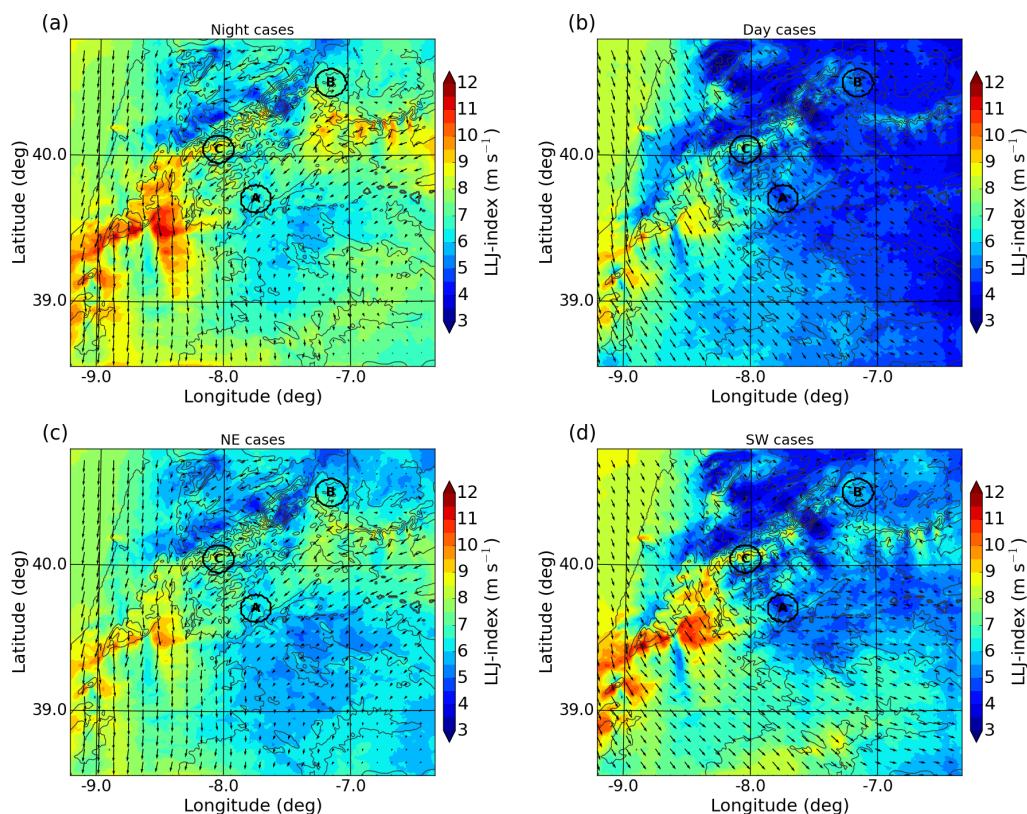
Figure 4. Temporal average of LLJ-index for the period 01 May to 15 June 2017. LLJs are detected by comparing wind speeds at 300 m AGL and 2000 m AGL during (a) night times (21 UTC to 9 UTC) and (b) day times (9 UTC to 21 UTC). In (c) and (d) only cases with wind directions from NE (negative cross-valley winds) and SW (positive cross-valley winds) at 300 m AGL at the location of the WT were used. Arrows show the mean wind field at 300 m AGL during (a) night-time, (b) day-time, (c) NE and (d) SW LLJ cases. Wind vectors are plotted on every 10th grid point. Areas marked by black circles and letters A to C indicate regions used for the computation of pressure and temperature gradients in cross- and along-valley direction (see text). Region A is centred at the location of the WT. The topography is indicated with thin black contour lines. Data is based on WRF domain D2.

During the second phase starting at about 23 May, the subtropical tropospheric jetstream has moved further north and the Iberian Peninsula was located under stable high pressure conditions. During this phase, cloud coverage and rain events decreased significantly while diurnal surface temperature variations and daily temperature maxima increased until the end of the campaign. In the free atmosphere, winds were weaker in comparison to the first phase and there were cases with non-western wind directions at 500 hPa (e.g., 23 May, 28 May, 12 June). Surface winds show a more frequently diurnal variation

of SW and NE winds compared to the first phase. This can be explained by the development of thermally driven wind systems,

115 which are favoured under weak synoptic conditions.

To analyse the occurence of LLJs during the campaign in more detail, the LLJ-index definition of Rife et al. (2010) for

nocturnal jets was used. This index is a measure for the strength of LLJs and is defined as:

$$\text{NLLJ} = \lambda\varphi\sqrt{[(\mathrm{u}_{00}^{\mathrm{L_1}} - \mathrm{u}_{00}^{\mathrm{L_2}}) - (\mathrm{u}_{12}^{\mathrm{L_1}} - \mathrm{u}_{12}^{\mathrm{L_2}})]^2 + [(\mathrm{v}_{00}^{\mathrm{L_1}} - \mathrm{v}_{00}^{\mathrm{L_2}}) - (\mathrm{v}_{12}^{\mathrm{L_1}} - \mathrm{v}_{12}^{\mathrm{L_2}})]^2}, \tag{1}$$

with zonal and meridional wind components u and v at vertical levels AGL $\mathrm{L_1}$ and $\mathrm{L_2}$ at local times (LT) 00 LT and 12 LT.

120 The binary masks λ and φ ensure nocturnal and jet-like wind profiles and are defined as:

$$\lambda = \begin{cases} 0, & \mathrm{ws}_{00}^{\mathrm{L_1}} \leq \mathrm{ws}_{12}^{\mathrm{L_1}} \\ 1, & \mathrm{ws}_{00}^{\mathrm{L_1}} > \mathrm{ws}_{12}^{\mathrm{L_1}}, \end{cases} \tag{2}$$

and

$$\varphi = \begin{cases} 0, & \mathrm{ws}_{00}^{\mathrm{L_1}} \leq \mathrm{ws}_{00}^{\mathrm{L_2}} \\ 1, & \mathrm{ws}_{00}^{\mathrm{L_1}} > \mathrm{ws}_{00}^{\mathrm{L_2}}, \end{cases} \tag{3}$$

with horizontal wind speed ws at level $\mathrm{L_1}$ and $\mathrm{L_2}$, respectively. As we were not only interested in night-time jets, we neglect

125 the coefficient λ and applied the following modified version of the LLJ-index based on hourly WRF D2 and D3 data:

$$\text{LLJ} = \varphi\sqrt{(\mathrm{u}^{\mathrm{L_1}} - \mathrm{u}^{\mathrm{L_2}})^2 + (\mathrm{v}^{\mathrm{L_1}} - \mathrm{v}^{\mathrm{L_2}})^2}, \tag{4}$$

with vertical levels $\mathrm{L_1}$=300 m AGL and $\mathrm{L_2}$=2000 m AGL. φ is defined as:

$$\varphi = \begin{cases} 0, & \mathrm{ws}^{\mathrm{L_1}} \leq \mathrm{ws}^{\mathrm{L_2}} \\ 1, & \mathrm{ws}^{\mathrm{L_1}} > \mathrm{ws}^{\mathrm{L_2}}, \end{cases} \tag{5}$$

In contrast to Rife et al. (2010) our LLJ-index is just based on wind speed differences between level $\mathrm{L_1}$ and $\mathrm{L_2}$ and not on

130 wind speed differences between night and day. This enables to compute the index for each hour of the day and compare LLJ-

indices during day- and night-time. Because of measured evidence and due to a higher horizontal and vertical grid resolution,

shallow LLJs are well represented in our model set-up and we therefore defined the levels $\mathrm{L_1}$ and $\mathrm{L_2}$ at lower altitudes than

Rife et al. (2010), who used $\mathrm{L_1}$=500 m AGL and $\mathrm{L_2}$=4000 m AGL with a horizontal model grid resolution of 4 km on 28

vertical levels. Figure 4(a) and (b) shows temporal averages of the LLJ-index for the period 01 May to 15 June 2017 for night-

135 and day-time. The computation of night-time LLJ-indices was based on averaging times between 21 UTC to 9 UTC, while

Atmospheric
Chemistry
and Physics
Discussions

10

day-times were averaged between 9 UTC to 21 UTC. This classification was used as nocturnal LLJs were often observed to

persist until after sunrise, while thermally driven winds from SW were observed until about 21 UTC. Note that local time in

Portugal is UTC+1h during the summer season. The spatial distribution of nocturnal LLJs in Fig. 4(a) shows that the strongest

nocturnal LLJs develop SW of Perdigão with a strong northerly flow down the slopes of the Serra da Estrela mountains towards

140 the flat Tejo-basin. In addition, strong jet winds developed NE of Perdigão over the slopes between the Serra da Estrela and

the Sierra de Gata mountain ranges and flowed down the basin of Castello Branco (see Fig. 1(b)) as a drainage flow towards

the double-ridge of Perdigão. Over the sea there is also a significant LLJ-index signal with mean winds from the North. This

flow is associated with the Azores anticyclone, which induces northerly winds parallel to the Portuguese coast line. During the

day the LLJ-activity is strongly reduced NE of Perdigão as can be seen in Fig. 4(b). SW of Perdigão and over the ocean, the

145 LLJ-index remains strong as during the night. In these regions, winds are blowing more from NW-directions during the day

compared to northerly winds during the night. This is probably due to the sea breeze effect, which impresses an onshore wind

component to the flow.

As the dominant wind directions for Perdigão are NE and SW winds, we additionally computed the mean LLJ-index for

cases when the cross-valley wind at the location of tower T20 next to the WT was negative at 300 m AGL (NE cases) and

150 for cases when it was positive (SW cases). The corresponding LLJ-index maps are shown in Fig. 4(c) and (d). The spatial

distribution of LLJs and the mean flow pattern during NE and SW cases is nearly identical to that during night and day cases,

respectively (Fig. 4(a) and (b)). This is confirmed by a correlation coefficient of 0.92 for the pointwise comparison of night

and NE LLJ-indices and by a correlation coefficient of 0.90 for day and SW cases. This indicates that on average, LLJs from

NE and SW over the double-ridge were respective night- and day-time phenomena although, exceptional cases with nighttime

155 LLJs from SW have also been observed (Wildmann et al., 2018a).

LLJ-indices were also computed for all radiosonde (RS) and wind profiler (WP) measurements during the campaign.

WRF D3 data were interpolated in space and time on the RS flight track and on the WP location before the LLJ-index was

calculated according to Eq. 4. Fig. 5 shows the direct comparison of simulated and observed mean LLJ-indices, which were

averaged for all, night/day and NE/SW cases, respectively. Both RS and WP data indicate that LLJs were strongest during

160 nighttime and during NE cases. The same result is obtained from WRF D3 simulations whose indices agree well with RS

and WP observations. LLJ-events occured during 30.0% (WRF: 23.5%) of all RS- and during 17.4% (WRF: 21.9%) of all

WP-observations during the campaign. Winds from NE at 300 m AGL (L1) were observed during 49.5% (WRF: 55.0%) of

RS- and during 42.0% (WRF: 55.1%) of WP-measurements. The observed LLJ frequency for NE cases was higher for RS

Atmospheric
Chemistry
and Physics
Discussions
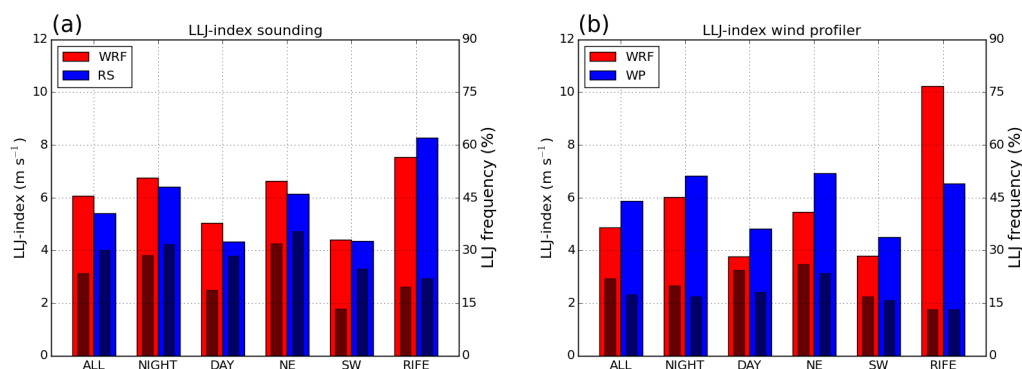
Figure 5. LLJ-indices obtained from (a) radiosonde (RS) launches and (b) wind profiler (WP) measurements during the campaign. WRF D3 indices were obtained by interpolating data in space and time on the radiosonde flight track and on the wind profiler location. Indices were averaged over the whole campaign period (ALL), the night and daytime (NIGHT, DAY) and for cases with wind directions from NE (negative) and SW (positive cross-valley winds at 300 m AGL). The nocturnal index according to the computation of Rife et al. (2010) is labeled with RIFE. The black bars indicate the frequency of LLJ occurence during all, night/day and NE/SW cases, respectively. For RIFE the black bars indicate the occurence of nocturnal jets during the whole campaign. See Fig. 1 for the wind profiler location and the launch site for soundings (every 6 h).

observations (35%, WRF: 32%) compared to WP-data (23%, WRF: 26%), as RS were launched within the valley (see Fig. 1) while the WP was located on the lee-side of the double-ridge. At tower T20, which is located on the SW ridge, LLJs did occur more frequently due to the elevated position during 42% of NE cases and during 30% of all synoptic conditions in the WRF D3 simulation (not shown). The original nocturnal NLLJ-index of Rife et al. (2010) (Eq. 1) was also computed and is labeled with RIFE in Fig. 5. NLLJ-values are slightly higher compared to our mean LLJ-indices probably as only one value per day is computed for NLLJ-indices by comparing the situation at 00 UTC and 12 UTC (see Eqs. 1 to 3). This results in a lower number of LLJ-events and a reduced smoothing when averaging is done over the whole campaign period. This can maybe explain the extreme high WRF NLLJ-index at the WP location.

To illustrate the daily changing flow patterns over the double-ridge in more detail, we plotted the simulated mean diurnal cycle of cross- and along-valley wind vertical profiles at the location of tower T20 in Fig. 6. In (a) and (b), averaging was done over the whole IOP from 01 May to 15 June 2017 and in (c) and (d) only for weak synoptic conditions. The latter were defined if the horizontal wind speed at an altitude of 3000 m was smaller than 10 m s^{-1} to reduce the effect of synoptic forcing on LLJ

Atmospheric
Chemistry
and Physics
Discussions

12

development. Cross-valley winds show a strong signal of nocturnal LLJs starting at about 21 UTC from northern directions

and with a maximum intensity between 6 UTC and 9 UTC from NE directions. During the day, a well mixed PBL develops

and mean winds turn to S and SW directions. At daytime no LLJ-structure is recognizable in the mean cross-valley wind. The

most interesting feature in the mean along-valley wind profiles is the wind component from NW (negative values) developing

180   during the evening transition starting at about 15 UTC with a maximum between 18 UTC and 21 UTC. This flow structure is

induced by downslope winds, which are generated after sunset over the steep slopes of the Estrela mountains NW of Perdigão

(see Fig. 1(b)). In the course of the night the flow over Perdigão turns from a NW to a N and a NE-flow due to the developing

down-valley LLJ along the Castello Branco basin (see Fig. 4(a)). During the morning transition a SE-flow develops into a S and

SW-flow during the day due to upslope and upvalley winds along the Estrela mountain slopes and along the Castello Branco

185   basin, respectively. This results in a clockwise diurnal wind turning near the surface.

To prove our hypothesis that the diurnal flow structures over Perdigão were dominated by thermally driven flows, we com-

puted horizontal gradients of potential temperature Θ and pressure in cross- and along-valley direction. Three circular regions

were defined in Fig. 4 with a diameter of 20 km that were centred at the wind turbine (region A), on the plateau between the

Serra da Estrela and Sierra de Gata mountains (region B) and on the steep slopes of the Serra da Estrela mountain range NW of

190   Perdigão (region C). For each region, time series of mean vertical potential temperature and pressure profiles were calculated,

which were then used to compute horizontal gradients between region A-B and region A-C. Mean diurnal vertical profiles of

these gradients are shown in Fig. 7 averaged over the whole campaign period. The difference of Θ between region A and B

shows higher temperatures between about 9 to 19 UTC and lower temperatures during the night over the elevated plateau in

region B (Fig. 7(a)). This can be explained by the valley volume effect (e.g., Wagner, 1938; Whiteman, 2000) and intensified

195   heating/cooling of the PBL over mountain slopes compared to the background atmosphere (Whiteman, 2000). This topograph-

ically induced differential warming/cooling leads to a horizontal pressure gradient, which is shown in Fig. 7(c) for the regions

A-B and forces a thermally driven SW-flow (higher pressure at region A) during the day and a NE-flow (higher pressure at

region B) during the night. A similar, but phase-shifted thermally driven flow system can be observed in along-valley direction

when comparing the regions A-C in Fig. 7(b) and (d). At late afternoon, the PBL over the steep slopes in region C is cooled

200   and downslope winds from NW directions develop. The positive pressure gradient remains throughout the night and changes

sign when the PBL is heated over the mountain slopes in region C after sunrise (Fig. 7(d)). The good agreement between

temperature, pressure and wind features in Fig. 6 and in Fig. 7 confirms the dominance of thermally driven flows during the

field campaign and can explain most of the observed LLJ events.

Atmospheric
Chemistry
and Physics
Discussions
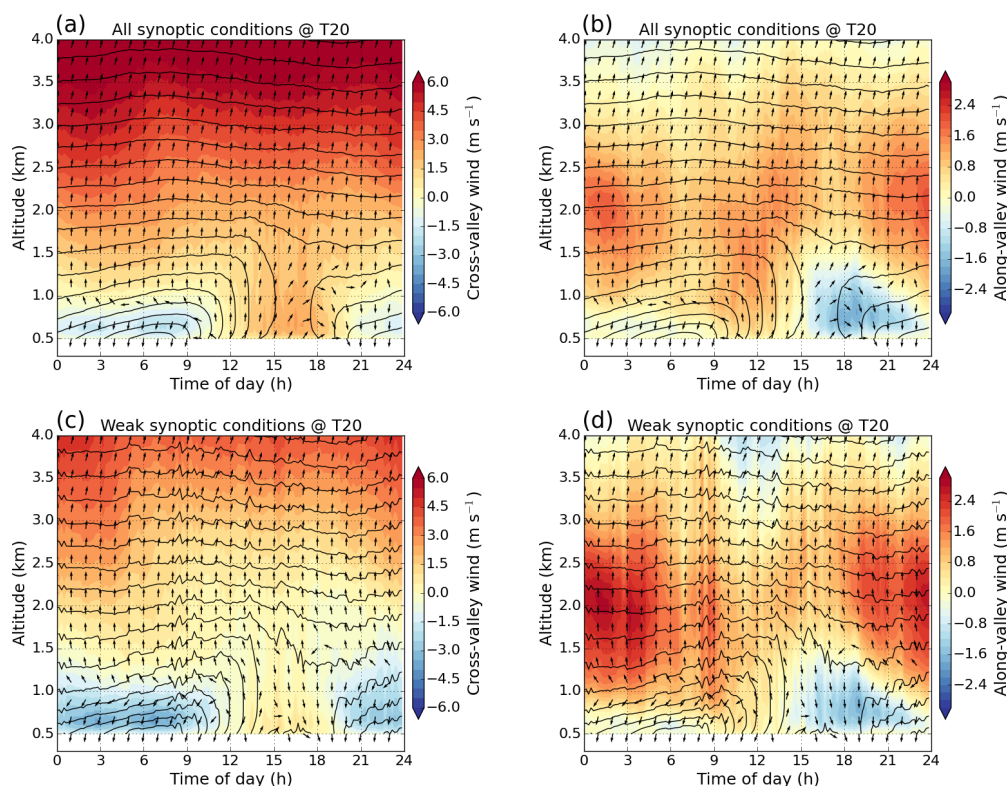
Figure 6. WRF D3 mean diurnal vertical profiles of (a) and (c) cross- and (b) and (d) along-valley wind at tower T20. The averaging period was 1 May to 15 June 2017. In (a) and (b) all data of this period were used for averaging, while in (c) and (d) only cases with weak synoptic conditions (defined by horizontal wind speeds < 10 m s^{-1} at 3000 m altitude) were utilized. Negative cross- (along-) valley winds indicate flow from NE (NW) directions, respectively. Black arrows show the mean horizontal wind direction (North=top). Black contour lines mark isentropes with a contour interval of 1 K.

4 Model verification

The dataset of remote and in-situ observations obtained during the Perdigão campaign enables to evaluate the long-term simu-
lations. Figure 8 and 9 show observed and simulated WRF D3 time series of cross- and along-valley wind at 100 m AGL at the
locations of tower T20, T25 and T29 (see Fig. 1 for the tower locations). The output interval of both data sets was 10 minutes.
Simulated cross- and along-valley winds show very good agreement with all three tower stations. Both absolute values and
phase of the observed signal are reproduced well by the model. It has to be recapitulated that the model was only initialized

Atmospheric
Chemistry
and Physics
Discussions

14
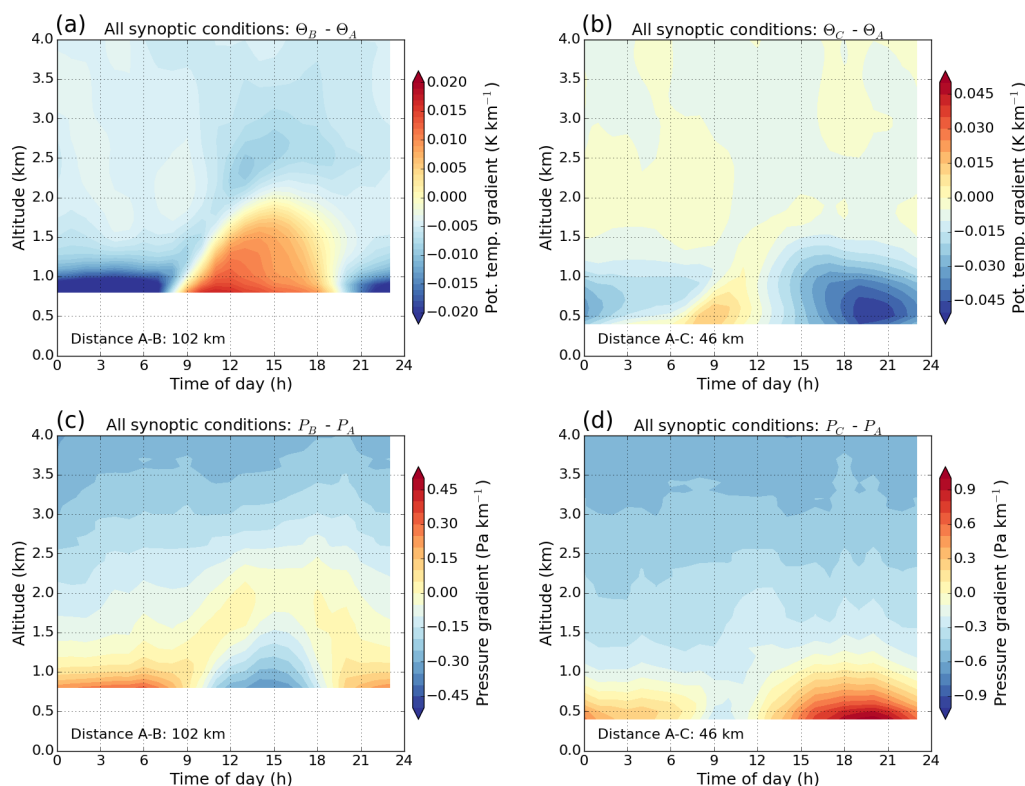
Figure 7. WRF D2 mean diurnal vertical profiles of horizontal potential temperature Θ and pressure P gradients between (a), (c) regions A and B and (b), (d) regions (A) and (C). The location of the regions is marked in Fig. 4. The averaging period was 1 May to 15 June 2017.

once and was run for a period of 49 days. The lateral boundaries of domain D1, where ECMWF data serve as boundary conditions, are 750 km away from the Perdigão site (see Fig. 1 (a)). Within the WRF domains the model develops its own dynamics and is capable to reproduce the diurnally changing flow systems during the whole simulation period with a surprisingly high quality. The comparison of tower T20 and T29 in Fig. 8(a) and (c) shows similar time series of cross-valley winds, as these towers were located on the SW and NE ridge, respectively and probed the PBL at the same altitude. Especially during phase II, diurnally changing NE and SW flow is visible from both T20 and T29 measurements and model simulations. Due to the location within the valley, Tower T25 in Fig. 8(b) shows much weaker cross-valley winds. Along-valley winds (Fig. 9) at T20 and T29 on the ridge tops are significantly lower than cross-valley winds on the ridge tops. In the valley at T25 along-valley winds seem to be the dominant wind component and reveal a diurnal changing NW and SE flow.

Atmospheric
Chemistry
and Physics
Discussions
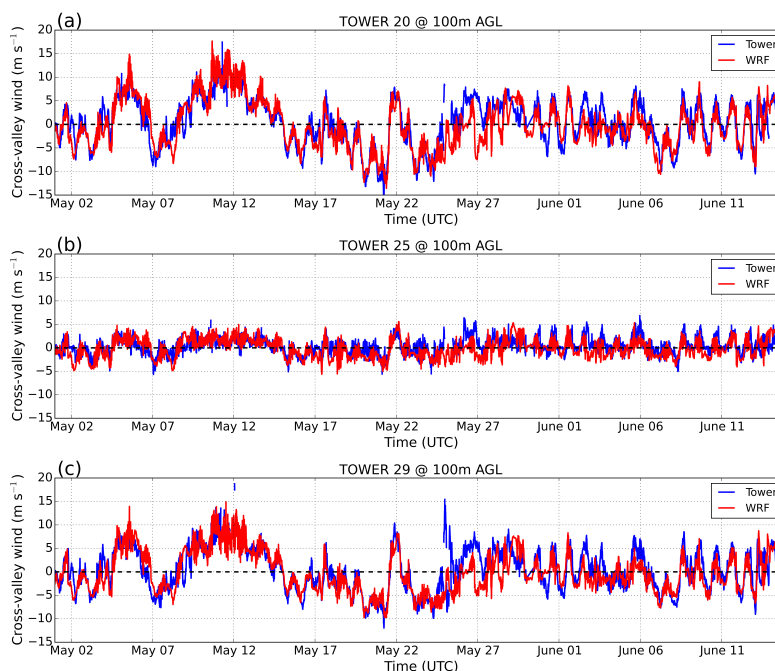
Figure 8. Time series of observed and simulated (WRF D3) cross-valley wind at 100 m AGL for (a) to (c) tower T20, T25 and T29 (see Fig. 1 (c) for tower locations).

To analyse the distribution of wind speed and direction at the three towers in a more quantitative way, corresponding wind roses are plotted in Fig. 10. The dominant wind directions at T20 and T29 on the two ridge tops were NE and SW. For these two sites the WRF model is in good agreement with observations. For T25 at the valley floor, the WRF model favours wind directions from NE, while observed directions show peaks for NW and SE wind directions. This means that the dominating along-valley flow at T25 is underestimated by the WRF model. Winds from NW-directions, which occur especially during the late afternoon due to downslope flow from the Estrela mountains were simulated by the WRF model especially under weak synoptic conditions (see Fig. 6(b) and (d)). These winds were, however, too weak as compared to observed winds in the valley. In addition, winds from S- and SE-directions, which occur mainly during the day were also significantly underestimated by the model at T25. The reason for underestimated along-valley flow is not clear and further sensitivity runs are necessary to investigate this issue.

As the simulation period was characterized by calm synoptic conditions (especially during phase II) and thermally driven flows played an important role, the daily distribution of cross- and along-valley winds at T20 and T25 is plotted in Fig. 11 and

16
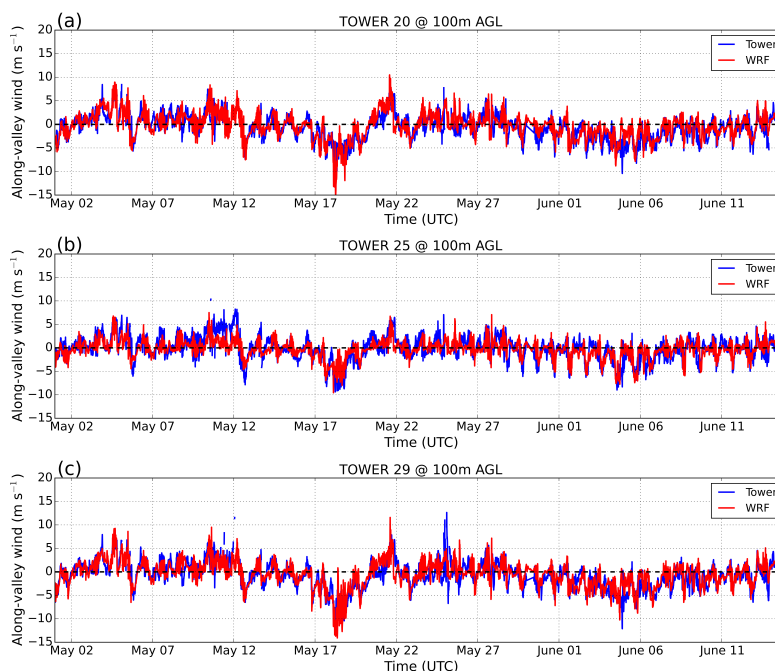
Figure 9. As in Fig. 8, but for the along-valley wind component.

Fig. 12. The most distinct feature in Fig. 11(a) and (b) is the sinusoidal cross-valley wind distribution at T20. This is induced

by nocturnal LLJs from NE and flow from SW at daytime. Cases with SW-flow during the night or NE-flow during the day

were synoptically driven events. Along-valley winds at T20 show less variation as compared to cross-valley winds, but there is

also a phase-shifted sinusoidal diurnal variation visible. Due to the influence of the Estrela mountains, minimum along-valley

235   winds (NW-flow) typically occured during the late afternoon as described already earlier in the text. This diurnal variation in

along-valley winds is more pronounced at T25 in the valley, as can be seen in Fig. 12(c) and (d). At this site, the along-valley

flow is the dominant flow feature. The comparison of observed and simulated along-valley winds in Fig. 12(c) and (d) shows

that the WRF model computes the measured diurnal cycle, but along-valley winds are generally too weak. This is in agreement

with the wind roses in Fig. 10(c) and (d). The simulated daily distribution of cross-valley winds at T20 and T25 is, however, in

240   good agreement with observed values.

Atmospheric
Chemistry
and Physics
Discussions
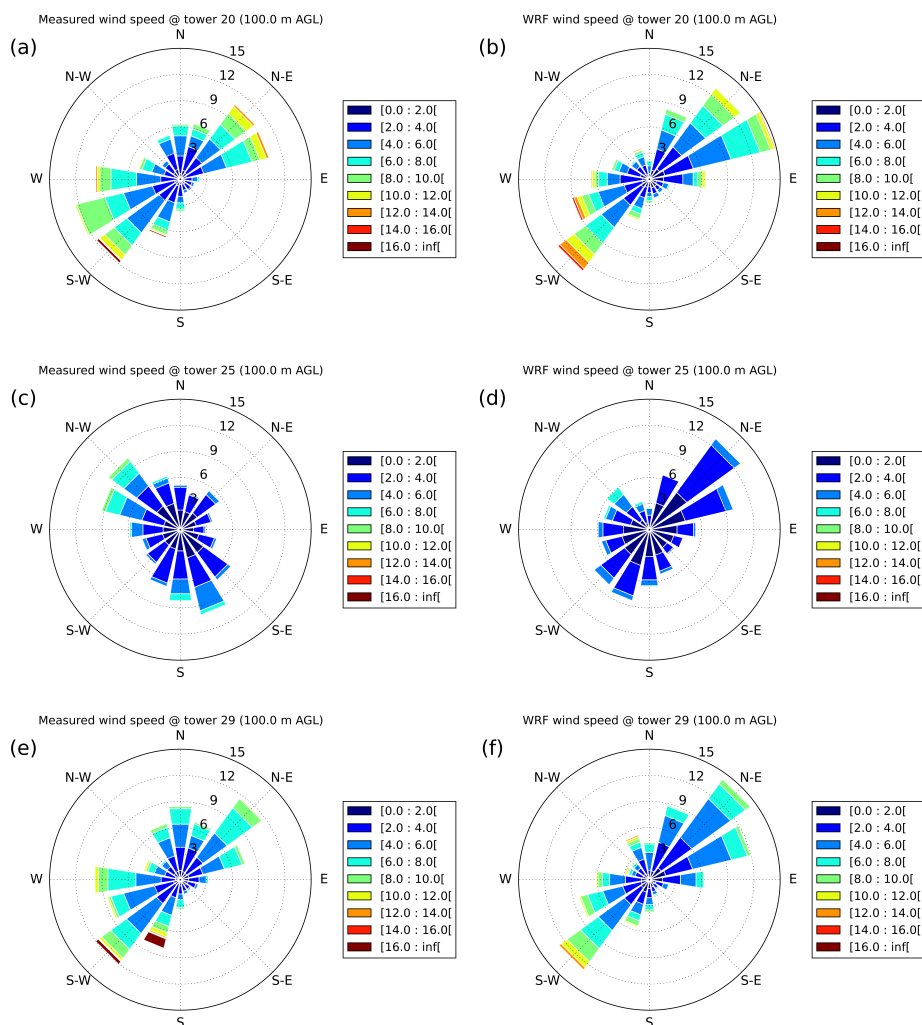
Figure 10. Wind distribution at 100 m AGL for observed (a), (c), (e) and simulated (b), (d), (f) WRF D3 winds at (a), (b) tower T20, (c), (d) T25 and (e), (f) T29 (see Fig. 1 (c) for tower locations).

5   Conclusions

Long-term WRF-LES simulations were performed with a horizontal resolution of 200 m for a period of 49 days during the Perdigão campaign in May and June 2017. Simulation results were used to characterize the meteorological conditions and to analyse characteristic flow patterns during the intensive observation period (IOP). The high grid resolution of 200 m was

18
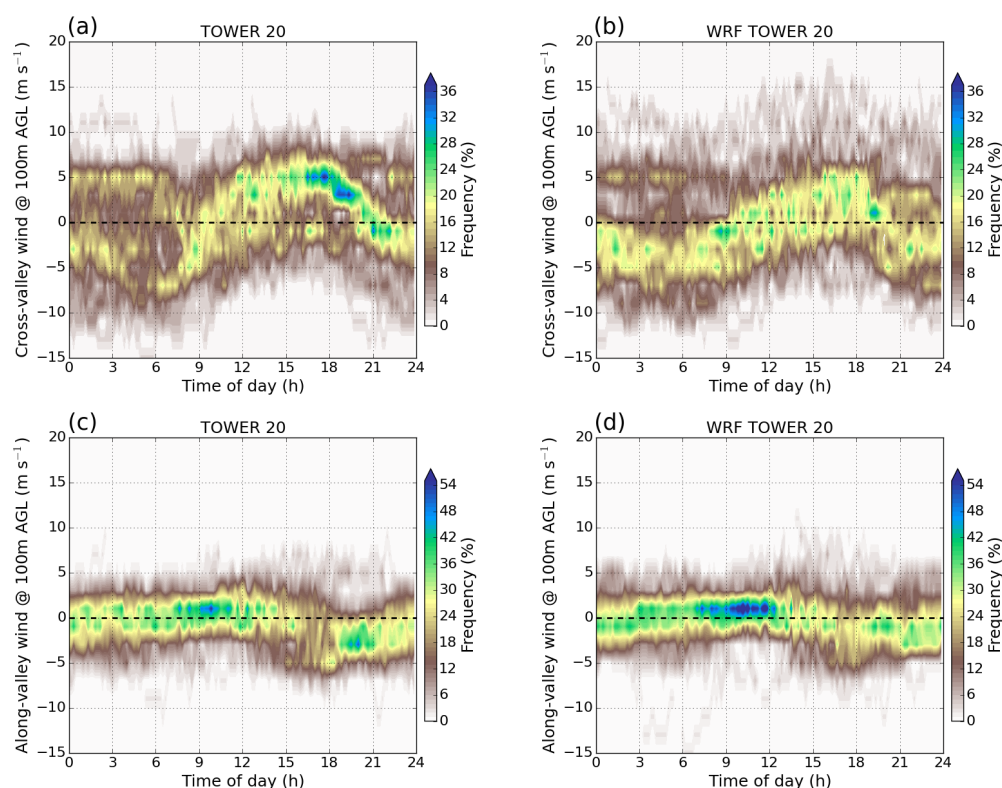
Figure 11. Diurnal distribution of (a) and (b) cross- and (c) and (d) along-valley wind at 100 m AGL at tower T20 in the period 1 May to 15 June 2017. Shown are observed tower data in (a) and (c) and data from WRF D3 simulations in (b) and (d).

necessary to resolve the double-ridge topography. Large parts of the campaign were dominated by synoptically calm conditions and the evolution of thermally driven flow systems (especially during the second half of the campaign). On the basis of the frequent observation of low-level jets (LLJ) by lidar and in-situ measurements a LLJ-index was computed following the method of Rife et al. (2010) to show that nocturnal LLJs from NE predominantly developed over the steep slopes between the Portuguese Serra da Estrala and the Spanish Sierra de Gata mountain ranges. This katabatic flow intensified during the night and moved down the broad basin of Castello Branco towards the double-ridge site of Perdigão. During the day, SW winds dominated. Due to the well mixed PBL, this flow had no LLJ-character in most cases. The computation of mean daily cycles of wind direction and cross-valley wind at T20 showed a diurnal clockwise wind turning near the surface with nocturnal LLJs from NE, S- and SW-winds during the day and NW- and N-flow in the evening transition due to downslope winds from the northern Estrela mountain range. This wind turning was also measured by in-situ and lidar instruments. The computation of
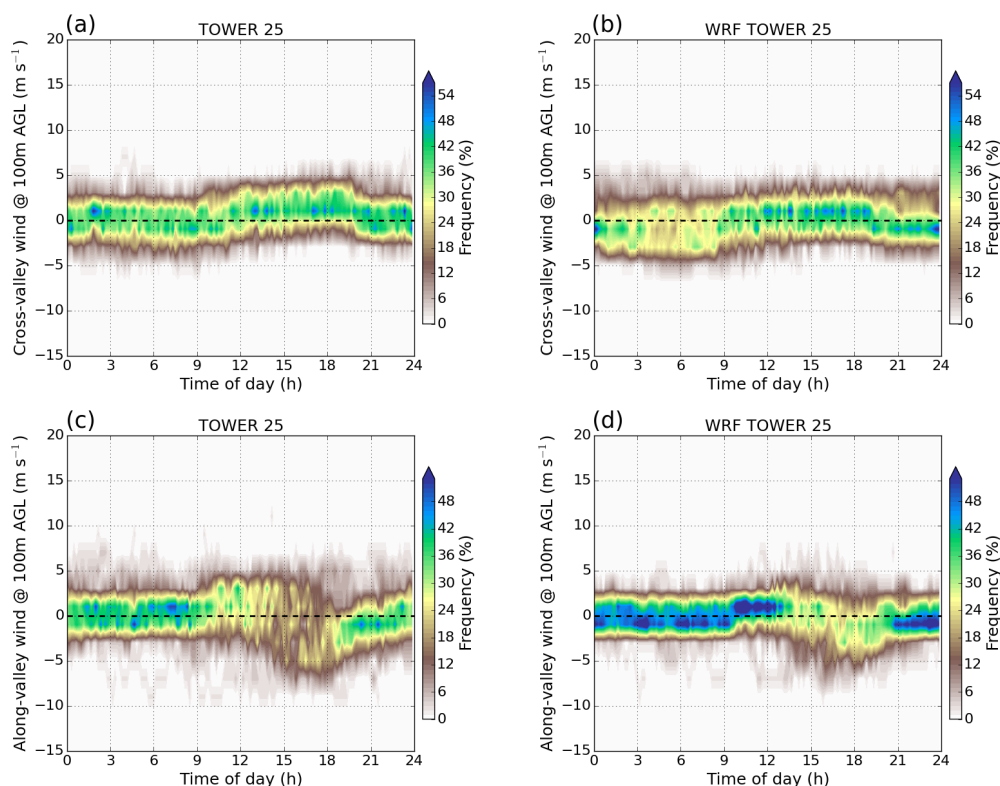
Figure 12. As in Fig. 11, but for tower T25 at the valley floor.

potential temperature and pressure gradients in cross- and along-valley direction confirmed the hypothesis that thermally driven flows dominated the atmospheric conditions in the PBL during the campaign period.

The verification of the model with in-situ observations showed a surprisingly good agreement in spite of the long simulation horizon of 49 days. Especially the diurnal changing flow from NE during the night and from SW during the day was captured well by the model on the ridges of the double-hill. In the valley, observations showed that along-valley winds were the dominating flow regime. WRF simulations computed these along-valley winds, but underestimated the strength of this flow significantly. The reason for this underestimation is not clear, but could possibly be improved by enhanced landuse data sets and increased grid resolution. This has to be tested in further sensitivity runs. The usage of additional roughness elements, such as the applied forest parameterization, will definitely be necessary for future real-case LES simulations to perform realistic model results.

Atmospheric
Chemistry
and Physics
Discussions

20

Atmospheric
Chemistry
and Physics
Discussions

Open Access

References

Banta, R. M., Darby, L. S., Fast, J. D., Pinto, J. O., Whiteman, C. D., Shaw, W. J., and Orr, B. W.: Nocturnal low-level jet in a mountain basin complex. Part I: Evolution and effects on local flows, J. Appl. Meteor., 43, 1348–1365, doi:10.1175/JAM2142.1, 2004.

Chen, F. and Dudhia, J.: Coupling an advanced land surface-hydrology model with the Penn State-NCAR MM5 modeling system. Part I: Model implementation and sensitivity, Mon. Wea. Rev., 129, 569–585, doi:10.1175/1520-0493(2001)129<0569:CAALSH>2.0.CO;2, 2001.

Daniels, M. H., Lundquist, J. K., Mirocha, J. D., Wiersema, D. J., and Chow, F. K.: A new vertical grid nesting capability in the Weather Research and Forecasting (WRF) model, Mon. Wea. Rev., 144, 3725–3747, doi:10.1175/MWR-D-16-0049.1, 2016.

Deardorff, J. W.: Stratocumulus-capped mixed layers derived from a 3-dimensional model, Bound.-Layer Meteor., 18, 495–527, doi:10.1007/BF00119502, 1980.

Dudhia, J.: Numerical study of convection observed during the winter monsoon experiment using a mesoscale two-dimensional model, J. Atmos. Sci., 46, 3077–3107, doi:10.1175/1520-0469(1989)046<3077:NSOCOD>2.0.CO;2, 1989.

Emeis, S.: Wind energy meteorology: Atmospheric physics for wind power generation, Springer, 2013.

Fernando, H. et al.: The Perdigão experiment: Peering into microscale details of mountain winds., Bull. Amer. Meteor. Soc., in preparation, 2018.

Hong, S.-Y. and Lim, J.-O. J.: The WRF single-moment 6-class microphysics scheme (WSM6), J. Korean Meteor. Soc., 42, 129–151, 2006.

Hong, S.-Y., Dudhia, J., and Chen, S.-H.: A revised approach to ice microphysical processes for the bulk parameterization of clouds and precipitation, Mon. Wea. Rev., 132, 103–120, doi:10.1175/1520-0493(2004)132<0103:ARATIM>2.0.CO;2, 2004.

Hong, S.-Y., Noh, Y., and Dudhia, J.: A new vertical diffusion package with an explicit treatment of entrainment processes, Mon. Wea. Rev., 134, 2318–2341, doi:10.1175/MWR3199.1, 2006.

Kain, J. S. and Fritsch, J. M.: A one-dimensional entraining/ detraining plume model and its application in convective parameterization, J. Atmos. Sci., 47, 2784–2802, doi:10.1175/1520-0469(1990)047<2784:AODEPM>2.0.CO;2, 1990.

Klemp, J. B., Dudhia, J., and Hassiotis, A. D.: An upper gravity-wave absorbing layer for NWP applications, Mon. Wea. Rev., 136, 3987–4004, doi:10.1175/2008MWR2596.1, 2008.

Mann, J. et al.: Complex terrain experiments in the New European Wind Atlas, Phil. Trans. R. Soc., 375, doi:10.1098/rsta.2016.0101, 2017.

Mlawer, E. J., Taubman, S. J., Brown, P. D., Iacono, M. J., and Clough, S. A.: Radiative transfer for inhomogeneous atmospheres: RRTM, a validated correlated-k model for the longwave, J. Geophys. Res., 102, 16 663–16 682, doi:10.1029/97JD00237, 1997.

Monaghan, A., Rife, D. L., Pinto, J. O., Davis, C. A., and Hannan, J. R.: Global precipitation extremes associated with diurnally varying low-level jets, J. Clim., 23, 5065–5084, doi:10.1175/2010JCLI3515.1, 2010.

Atmospheric
Chemistry
and Physics
Discussions

Open Access

EGU

22

300 Pineda, N., Jorba, O., Jorge, J., and Baldasano, J. M.: Using NOAA AVHRR and SPOT VGT data to estimate surface parameters: application to a mesoscale meteorological model, Int. J. Remote Sensing, 25, 129–143, doi:10.1080/0143116031000115201, 2004.

Rife, D. L., Pinto, J. O., Monaghan, A. J., Davis, C. A., and Hannan, J. R.: Global distribution and characteristics of diurnally varying low-level jets, J. Clim., 23, 5041–5064, doi:10.1175/2010JCLI3514.1, 2010.

Schmugge, T. J., Abrams, M. J., Kahle, A. B., Yamaguchi, Y., and Fujisada, H.: Advanced spaceborne thermal emission and reflection
305 radiometer (ASTER), Remote Sensing for Agriculture, Ecosystems and Hydrology, 4, doi:10.1117/12.469693, 2003.

Schulz, C., Klein, L., Weihing, P., Lutz, T., and Krämer, E.: CFD studies on wind turbines in complex terrain under atmospheric inflow conditions, J. Phys.: Conf. Ser., 524, 012 134, doi:10.1088/1742-6596/524/1/012134, 2014.

Shaw, T. H. and Schumann, U.: Large-eddy simulation of turbulent flow above and within a forest, Bound.-Layer Meteor., 61, 47–64, doi:10.1007/BF02033994, 1992.

310 Skamarock, W. C., Klemp, J. B., Dudhia, J., Gill, D. O., Barker, D. M., Duda, M. G., Huang, X.-Y., Wang, W., and Powers, J. G.: A description of the Advanced Research WRF Version 3, NCAR technical note, Mesoscale and Microscale Meteorology Division, National Center for Atmospheric Research, Boulder, Colorado, USA, http://www2.mmm.ucar.edu/wrf/users/docs/arw_v3.pdf, 2008.

Storm, B., Dudhia, J., Basu, S., Swift, A., and Giammanco, I.: Evaluation of the Weather Research and Forecasting Model on forecasting low-level jets: Implications for wind energy, Wind Energy, 12, 81–90, doi:10.1002/we.288, 2009.

315 Tian, W., Ozbay, A., Yuan, W., Sarakar, P., and Hu, H.: An experimental study on the performances of wind turbines over complex terrain, in: 51st AIAA Aerospace sciences meeting including the new horizons forum and aerospace exposition, 07-10 January 2013, Grapevine, Texas, USA, pp. 1–14, doi:10.2514/6.2013-612, 2013.

UCAR/NCAR - Earth Observing Laboratory: NCAR/EOL Preliminary 5 minute ISFS data, geographic coordinate sonic winds, not tilt corrected. Version 0.2 [PRELIMINARY]. UCAR/NCAR - Earth Observing Laboratory, https://data.eol.ucar.edu/dataset/536.011, accessed
320 03 Sep 2018, 2017a.

UCAR/NCAR - Earth Observing Laboratory: NCAR/EOL 1290MHz Wind Profiler NIMA Winds and RASS Data. Version 1.0. UCAR/NCAR - Earth Observing Laboratory, doi:10.5065/D6RB73BK, accessed 03 Sep 2018, 2017b.

UCAR/NCAR - Earth Observing Laboratory: NCAR/EOL Quality Controlled Radiosonde Data. Version 2.0. UCAR/NCAR - Earth Observing Laboratory, doi:10.5065/D6H70DM1, accessed 03 Sep 2018, 2018.

325 Wagner, A.: Theorie und Beobachtung der periodischen Gebirgswinde, Gerlands Beitr. Geophys., 52, 408–449, 1938.

Whiteman, C. D.: Mountain meteorology: Fundamentals and applications, Oxford University Press, 2000.

Wildmann, N., Kigle, S., and Gerz, T.: Coplanar lidar measurement of a single wind energy converter wake in distinct atmospheric stability regimes at the Perdigão 2017 experiment, J. Phys.: Conf. Ser., 1037, doi:10.1088/1742-6596/1037/5/052006, 2018a.

Wildmann, N., Vasiljevic, N., and Gerz, T.: Wind turbine wake measurements with automatically adjusting scanning trajectories in a multi-

330   Doppler lidar setup, Atmos. Meas. Tech., 11, 3801–3814, doi:10.5194/amt-2018-55, 2018b.